Atmospheric Research 293 (2023) 106919

Contents lists available at ScienceDirect

Atmospheric Research

journal homepage: www.elsevier.com/locate/atmosres

Radiative heating and upwelling by different types of TTL clouds over the tropical convective regions

Siliang Lei [a,b], Byung-Ju Sohn [a,c], Joowan Kim [d], Chao Liu [a,b,*]

[a] Collaborative Innovation Center on Forecast and Evaluation of Meteorological Disasters/China Meteorological Administration Aerosol-Cloud-Precipitation Key Laboratory, School of Atmospheric Physics, Nanjing University of Information Science & Technology, Nanjing 210044, China
[b] Innovation Center for FengYun Meteorological Satellite (FYSIC), National Satellite Meteorological Center (National Center for Space Weather), Beijing 100081, China
[c] School of Earth and Environmental Sciences, Seoul National University, Seoul 08826, South Korea
[d] Department of Atmospheric Science, Kongju National University, Gongju 32588, South Korea

ARTICLE INFO

Keywords:
Tropical tropopause layer
TTL cloud
Cloud property
Cloud radiative heating
Cloud-induced upwelling

ABSTRACT

Tropical tropopause layer (TTL) clouds, defined as clouds whose tops are located above the tropopause level, play important roles in Earth's radiation balance and troposphere-to-stratosphere transport. Examining how different TTL cloud type gives influence on the radiative heating, we classified TTL clouds into three types (i.e., deep convective cloud, optically thick convective anvil cloud, and optically thin cirrus cloud) over the convectively active four tropical regions (i.e., Central Africa and South America continental regions and the Central and Western Pacific oceanic regions), using the combined Cloud-Aerosol Lidar and Infrared Pathfinder Satellite Observations (CALIPSO) and CloudSat data. Using the classified cloud data, we first examined characteristics of the macrophysical and microphysical properties of the classified cloud types. Amongst three types of TTL clouds over selected four regions, thin cirrus clouds are most abundant (almost four-fifths), and approximately 7% and 17% of TTL clouds are deep convective cloud and thick convective anvil clouds, respectively. It is noted that the land–ocean contrast in TTL clouds appears weak in spite of well-known land–ocean contrast in the convection intensity, suggesting that TTL cirrus clouds may be dominated by in situ cirrus clouds. We further examined radiative heating over the TTL altitudes by each cloud type and the associated radiatively-driven upwelling motion. It is revealed that the dominant contribution to the overall radiative heating is from thin cirrus clouds (~48.4%) because of their abundance. Nevertheless, convective anvil clouds and deep convective clouds are also found to give significant contribution to the radiative heating. Such cloud radiative heating tends to lower the level of zero net radiative heating rate found in the clear sky by ~400–900 m. The TTL clouds play an important role in the secondary circulation in the TTL by inducing the upwelling motion throughout the TTL, supporting the mechanism that the radiative effect of TTL clouds can enhance the mass flux from the troposphere to the stratosphere.

1. Introduction

It is well known that the tropopause separating the turbulent troposphere from the stable stratosphere is a transition layer rather than a material surface (Fueglistaler et al., 2009). Over the tropics, this transition layer extending from the upper troposphere to the lower stratosphere is called the tropical tropopause layer (TTL). Over the tropics, deep convection reaches the TTL, providing cloud hydrometeors as well as water vapor to the TTL, playing as an important source of TTL clouds. In general, TTL clouds are composed of deep convective clouds (DCCs), convectively detrained optically thick anvil clouds, optically thin cirrus clouds from dissipating anvil clouds, and optically thin in situ cirrus clouds (Lawson et al., 2019; Garrett et al., 2004). Thus, the TTL cirrus clouds are from two sources, and their contributions to the total cirrus clouds are nearly same (Heymsfield and Donner, 1990; Luo and Rossow, 2004).

The TTL also corresponds to the transition layer from radiative cooling in the troposphere to radiative heating in the stratosphere (Haladay and Stephens, 2009; Gettelman et al., 2004), and the TTL clouds play an important role in shaping the vertical radiative cooling/

* Corresponding author at: Collaborative Innovation Center on Forecast and Evaluation of Meteorological Disasters/China Meteorological Administration Aerosol-Cloud-Precipitation Key Laboratory, School of Atmospheric Physics, Nanjing University of Information Science & Technology, Nanjing 210044, China.
E-mail address: chao_liu@nuist.edu.cn (C. Liu).

https://doi.org/10.1016/j.atmosres.2023.106919
Received 4 November 2022; Received in revised form 2 July 2023; Accepted 7 July 2023
Available online 16 July 2023

heating structure in the TTL, especially by lowering the level of zero net radiative heating rate (Corti et al., 2005, 2006). In addition to the ability of TTL clouds to alter the heat balance in the TTL, they can also induce cloud lofting (i.e., diabatic lift of the cloud layer) (Jensen et al., 1996) and facilitate the upwelling motion in the TTL through enhanced cloud radiative heating, helping to transport trace gases from the troposphere to the stratosphere (Corti et al., 2005, 2006). Thus, characterization of cloud properties and cloud-induced radiative heating should be important for understanding the mechanism to control the physical processes in the TTL. However, despite recent findings regarding TTL clouds, the detailed cloud structures (both horizontally and vertically) are not well described partly because of the lack of observations.

Recent advances in satellite measurement technologies and remote sensing capabilities have enabled the examination of more detailed features of TTL cloud properties. In particular, the Cloud-Aerosol Lidar and Infrared Pathfinder Satellite Observations (CALIPSO) data have provided detailed information on cloud properties in the TTL (Virts and Wallace, 2010; Virts et al., 2010; Yang et al., 2010; Tseng and Fu, 2017). However, most of those studies are based on relatively crude definitions of TTL clouds. For example, Tseng and Fu (2017) examined the spatial and temporal features of TTL cirrus clouds using CALIPSO-only observations, and cirrus clouds were defined as clouds with bases higher than 14.5 km in altitude. However, the lidar signal of CALIPSO is depleted quickly in cloudy conditions; hence, the reflected lidar signal becomes quickly saturated in the case of optically thick clouds, such as anvil clouds and DCCs. The maximum optical thickness of cloud that can be measured by the CALIPSO lidar is only approximately 3–5 (Winker et al., 2010). Thus, the cirrus clouds determined by the cloud base from CALIPSO observations only may include convectively-driven anvil clouds and deep convective plumes because CALIPSO lidar is likely to measure only the uppermost part of those clouds. Meanwhile, the use of fixed tropopause height (TH) for determining TTL clouds over different regions and seasons is also questionable. Therefore, how much/where each type of TTL cloud exists, how their vertical structures appear, how those TTL clouds are linked to convective clouds below the tropopause level, or how much the individual cloud contributes to the net cloud radiative heating are less known.

Over the tropics, TTL clouds are largely confined within specific regions, i.e., Central Africa (CA), South America (SA), and the Central and Western Pacific (CP and WP) (Yang et al., 2010). Note that the CA and SA represent the continental deep convective regions, and the CP and WP represent the oceanic deep convective regions. Aircraft and satellite observations indicate that continental convection intensity is much stronger than that over ocean (Matsui et al., 2016; Heymsfield et al., 2010; Lucas et al., 1994; Zipser et al., 2006). The convection intensity over land can be 2 to 3 times stronger than that over ocean (Lucas et al., 1994). Even in the upper troposphere, the updrafts within clouds over land are stronger than those over ocean by a factor of approximately 1.5 (Jeyaratnam et al., 2021). Given the fact that the WP warm pool region is the dominant source region for the tropospheric air entering the stratosphere (Fueglistaler et al., 2004), a natural question might arise, such as what role does the oceanic convection play in the TTL circulation and mass transport. It is also interesting to examine how cloud property and radiative heating are in contrast between land and ocean in TTL because there is strong land–ocean contrast in convection intensity and thus we may expect the similar contrast even in the TTL layer.

Moreover, clouds are byproducts of underlying atmospheric circulation, while the resultant clouds themselves can modify the circulation through changes in the radiative heating field (Sohn, 1999; Hartmann et al., 2001; Gettelman, 2004; Mauritsen et al., 2013; Harrop and Hartmann, 2016). Thus, TTL clouds can provide feedback on the underlying circulation that is responsible for their existence. How TTL clouds can alter the radiative heating fields and their consequences for circulation and mass transport have been examined (Fu et al., 2018; Corti et al., 2005). With the concept of cloud's radiatively driven circulation change, Corti et al. (2006) further proposed a mechanism that cirrus-induced radiative heating in the TTL can enhance the upwelling there, supplying sufficient air to feed the low branch of the Brewer-Dobson circulation. Given the importance of cloud-induced radiative heating in the TTL circulation, it should be worth examining how radiative heating is maintained or how much radiative heating is contributed by different cloud types (e.g., DCCs, anvil clouds, and cirrus clouds).

With all the aforementioned importance of TTL clouds in the radiative heating and associated upwelling in TTL, this study intends to separate the TTL clouds into DCCs, convectively detrained optically thick/thin anvil clouds, and optically thin cirrus clouds over the selected four tropical convection regions (CA, SA, CP and WP), to document the climatological features, such as the vertical extent, cloud height, and occurrence frequency for different cloud types. In doing so, CALIPSO and CloudSat data are combined to obtain the vertical structure of each TTL cloud type. The vertical radiative heating distributions for different cloud types are also obtained and converted into their respective vertical motions to examine how the radiative heating induced upwelling motion in the TTL might be linked to the mechanism of transporting air from the troposphere to the stratosphere. This approach is thought to be novel because the climatology of various physical properties for different TTL cloud types and their link to the TTL upwelling have not been studied, despite their importance.

The rest of the paper is organized as follows. Section 2 introduces observations and methods for TTL cloud classifications and their radiative heating. The results of the averaged properties of different kinds of TTL clouds are presented in Section 3. Section 4 discusses cloud radiative heating and induced vertical velocity and reveals the corresponding results. Section 5 summarizes and discusses this work.

2. Data and methodology

2.1. Observational and reanalysis data

Satellite observations from the A-Train constellation (Stephens et al., 2002) are used to obtain TTL cloud properties and to extract cloud vertical profiles; we use four years of observations from 2007 to 2010 from two active instruments, i.e., the Cloud-Aerosol Lidar with Orthogonal Polarization (CALIOP; Winker et al., 2010) onboard CALIPSO and the CloudSat Cloud Profiling Radar (CPR; Stephens et al., 2008). CALIOP observations with a 5 km pixel resolution are used, and their vertical resolutions are 60 m and 180 m below and above 20.2 km altitude, respectively. The CPR footprint size is 2.3 km along track and 1.4 km cross track (Winker et al., 2010), and the CPR product gives oversampled profiles with a vertical resolution of 240 m. More importantly, CALIOP detects only optically thin clouds while CPR is not designed for detecting such optically thin clouds but rather for optically thick clouds. Thus, this study considers both CPR and CALIOP observations of four years from 2007 to 2010 for the TTL classification and cloud property studies, which are described in detail in the following subsection.

To better identify TTL clouds, we use local THs from the CALIOP 5 km pixel resolution cloud profile product (05kmCPro product; Vaughan et al., 2018), and the data are based on the Global Modeling and Assimilation Office Goddard Earth Observing System Model version 5 (GEOS-5), whose uncertainties are reported to be approximately 140 m for the TH (Pan and Munchak, 2011). Moreover, the atmospheric temperature and specific humidity used for the vertical velocity calculation are from CloudSat ECMWF_AUX product (Cronk and Partain, 2017), which is based on the collocated European Centre for Medium-Range Weather Forecast reanalysis data, i.e., AN-ECMWF.

2.2. TTL clouds and classifications

TTL clouds are generally referred to as clouds around the tropopause.

We use the variable TH as a threshold to identify TTL clouds because TH varies with latitude, region, and season (Tegtmeier et al., 2020). In this study, TTL clouds are defined as cloudy pixels with the cloud top height (CTH) above the local TH. Based on this definition, this study mainly focuses on overshooting convective clouds and associated anvil and cirrus clouds whose CTHs are above the local TH. Moreover, TH is directly extracted from GEOS-5, and more details regarding the TH and its accuracy are found in previous studies (Rienecker, 2008; Pan and Munchak, 2011; Tseng and Fu, 2017). There may be inevitable bias due to the vertical resolution of the observations in the TTL, i.e., approximately the order of ~100 m, leading to some TTL clouds being excluded and some unreasonable pixels (high stratospheric feature or low middle-level clouds) being included (Tegtmeier et al., 2020; Xian and Homeyer, 2019). To reduce bias, we remove some unreasonable pixels with TH lower than 13 km and higher than 21 km, which account for less than 1% of all available data.

Collocated CALIOP and CPR cloud profiles are combined to give a full picture of vertical cloud distribution for each pixel. In other words, the vertical grid detected either by CALIOP (i.e., CALIOP vertical feature mask) or CPR (2B-CLDCLASS product) is marked as cloudy, so both optically thin layers missed by CPR and the lower layers of optically thick clouds missed by CALIOP are accounted for. From this combined cloud profile, it is now straightforward to determine corresponding CTH, cloud base height (CBH), and cloud depth (CD, the difference between CTH and CBH).

Moreover, cloud profiles and CALIOP-derived ice water path (IWP) are used for classifying TTL clouds into three types. The classification method that we apply is described by Sokol and Hartmann (2020). In a convective system, it was assumed that the probability trend of the IWP has a physical meaning; thus, the variable IWP could be used as a benchmark to identify optically thick anvil clouds and optically thin cirrus clouds. Sokol and Hartmann (2020) use the raDRA-liDAR cloud (DARDAR-CLOUD) dataset assimilated by the combined CALIOP and CPR observations (Delanoë and Hogan, 2010; Ceccaldi et al., 2013) to obtain the key IWP parameter. Different from the DARDAR-CLOUD dataset, we use the IWP only from CALIOP observations, which is considered sufficient to distinguish thin cirrus clouds from optically thick anvil clouds. Fig. 1 shows the probability distribution of the CALIOP-derived IWP. The dashed line indicates the separation between optically thick anvil clouds and optically thin cirrus clouds, so the corresponding threshold of IWP = 10 g/m^2 suggested by Sokol and Hartmann (2020) is used for separating optically thick anvil clouds from thin cirrus clouds. Note that the CALIOP-derived IWP here represents only that of the uppermost layer, but it is sufficient to extract those optically thin cirrus clouds.

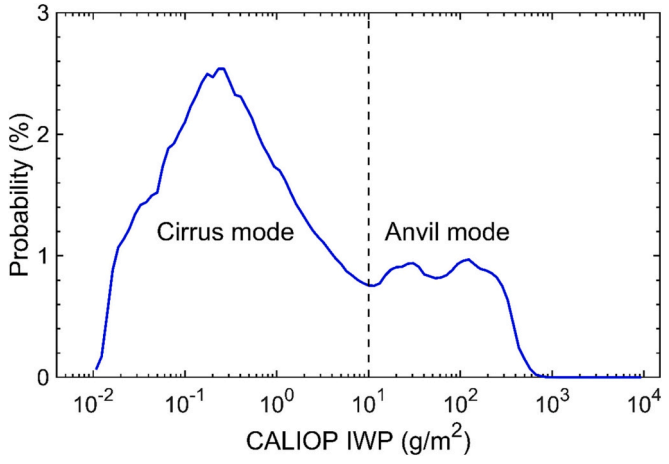

Fig. 1. Probability distribution of ice water paths (IWPs) based on the Cloud-Aerosol Lidar with Orthogonal Polarization (CALIOP) from 2007 to 2010.

After extracting all TTL cloudy pixels, the cloud classification is achieved by following three steps. First, pixels with CBHs below 5 km in altitude, i.e., corresponding to the average freezing level, are defined as DCCs. Thus, the DCCs in our classification represent only those from convective cores. Second, cirrus clouds are defined as those with IWPs in the uppermost cloud layer smaller than 10 g/m^2 amongst pixels remained after screening out DCCs. Lastly, the remaining pixels, whose CBHs are higher than 5 km and uppermost layer IWPs are larger than 10 g/m^2, are considered to be optically thick anvil clouds. In this separation, since optically thick (IWP > 10 g/m^2) clouds are counted as anvil clouds, the thin cirrus clouds defined here are composed of in situ cirrus clouds plus thin cirrus clouds from dissipating convective anvil clouds. It has been noted that the TTL cirrus clouds originate from two different sources: in situ cirrus clouds and thin cirrus clouds from dissipating anvil clouds (Lawson et al., 2019).

In this analysis, separation is done at four regions showing abundant TTL clouds (or four convectively active tropical regions), which are referred to as Central Africa (CA: 20°S–8°N, 2°E–38°E), South America (SA: 20°S–6°N, 46°W–82°W), Central Pacific (CP: 20°S–12°N, 153°E–163°W), and Western Pacific (WP: 20°S–4°N, 107°E–153°E). Amongst them, CA and SA represent continental domains while CP and WP represent oceanic domains. Analysis is done during the winter seasons (December, January, and February) from 2007 to 2010 (i.e., total of 12 months) since there are abundant TTL clouds in the selected four domains with a clear land–ocean contrast during the winter time, as shown in Fig. 2 in the following Section 3.

2.3. Vertical velocity induced by TTL cloud radiative heating

Clouds can change the radiative balance and alter the existing vertical motion in the TTL through radiative heating or cooling. Thus, we investigate the cloud-induced radiative heating and derived vertical motion in the TTL and examine different contributions from different kinds of TTL clouds in different regions. Note that we investigate only TTL cloud contributions. Although the latent heating (Huaman and Schumacher, 2018; Chang and L'Ecuyer, 2019), eddy sensible heat flux and horizontal temperature advection (Yang and Smith, 2000) may also influence TTL, their magnitudes appear minor in comparison to the radiative heating. On the other hand, horizontal sensible heat advection is relatively small over the tropics because the horizontal temperature gradient near the tropopause level is small (Sobel et al., 2001).

Because of the dominance of radiative heating in the TTL, cloud-induced radiative heating is largely balanced with vertical motion (e.g., Yanai et al., 1973; Mapes and Houze, 1995; Olson et al., 1999; Corti et al., 2005), i.e.:

$$-S_p\omega_p = Q, \tag{1}$$

where S_p is the static stability, ω_p is the pressure vertical velocity, and Q is the cloud-induced radiative heating. In Eq. (1), S_p can be defined as follows:

$$S_p = -\left(\frac{T}{\theta}\right)\left(\frac{\partial\theta}{\partial p}\right), \tag{2}$$

where T and θ are the temperature and potential temperature, respectively, and p is the pressure. Thus, the vertical velocity can be readily obtained for a given radiative heating profile for each TTL cloudy pixel. Then, the average radiative heating rate and vertical velocity within a given region are obtained as follows:

$$Q_{avg} = \frac{\sum_{n=0}^{N} Q(n)}{N}, \tag{3}$$

$$\omega_{avg} = \frac{\sum_{n=0}^{N} \omega_p(n)}{N}. \tag{4}$$

Here, N indicates the total number of pixels for a certain cloud type

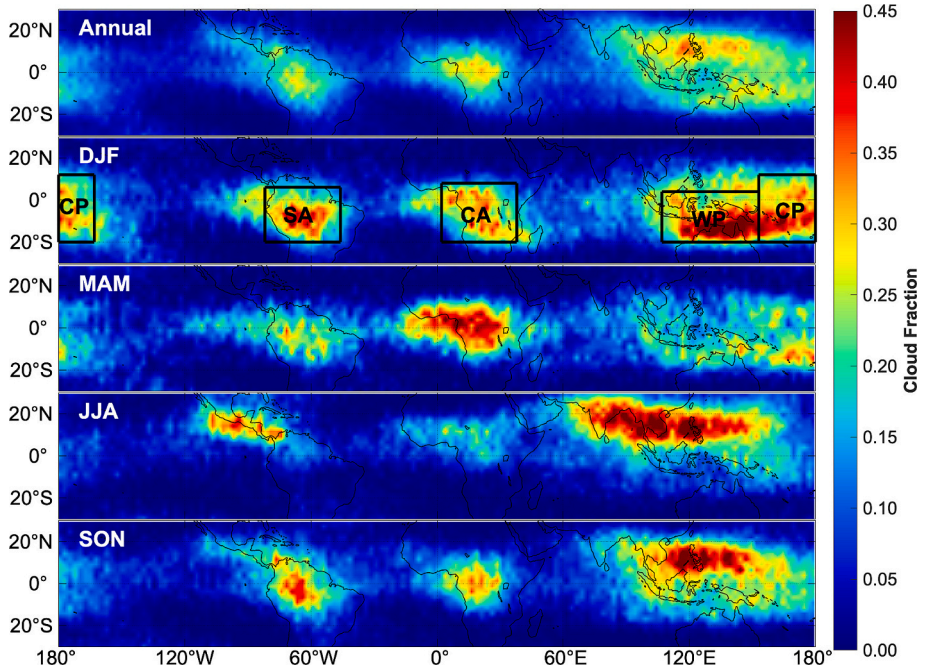

Fig. 2. Annual and seasonal spatial distributions of the tropical tropopause layer (TTL) cloud fraction given in a 2.5° × 2.5° grid resolution from 2007 to 2010. The top panel is for the annual result, and the following four panels are for boreal winter (DJF: December, January, and February), spring (MAM: March, April, and May), summer (JJA: June, July, and August) and fall (SON: September, October, and November).

within a given region, and $Q(n)$ and $\omega_p(n)$are the corresponding values of the nth pixel. Thus, Q_{avg} and ω_{avg} can be calculated for either TTL cloudy pixels or clear-sky pixels, and those values for TTL DCC, anvil and cirrus cloudy pixels can also be obtained separately. Thus, cloud impacts are obtained by taking the difference between cloud profiles and clear-sky profiles. In this calculation, the radiative heating in the cloudy pixel can be understood as the sum of clear-sky radiative heating and cloud-induced radiative heating. Thus, the cloud-induced heating $Q_{cld\_induced}$ within the cloudy pixel (i.e., the contribution due to the presence of clouds) can be expressed as follows:

$$Q_{cld\_induced} = Q_{cld} - Q_{clr}, \tag{5}$$

where Q_{cld} is the radiative heating for cloudy pixels calculated by Eq. (3), and Q_{clr} is for clear-sky conditions. Then, the vertical motion is inferred from Eq. (1) for the given radiative heating shown in Eq. (5).

The TTL cloud radiative heating is obtained from the joint CPR-CALIOP 2B-FLXHR-LIDAR product (Henderson et al., 2013), based on the radiative transfer calculation using a two-stream plane-parallel doubling-adding radiative transfer model with the vertical structure from joint CPR and CALIOP as inputs. The meteorological data, i.e., pressure and temperature, used for Eq. (2), are from AN-ECMWF as mentioned in Section 2.1.

3. TTL cloud properties

Fig. 2 gives the spatial distributions of annual and seasonal TTL cloud fractions in the tropics. The cloud fraction is given as a ratio of the number of pixels with TTL clouds to the number of total available pixels within a 2.5° × 2.5° grid. The four black boxes in the DJF (i.e., December, January, and February) map represent the selected four regions where TTL clouds occur frequently, i.e., CA, SA, CP and WP as defined in Section 2.2, and our following discussions focus on the averages over those four regions. The distributions in Fig. 2 show similar spatial distributions to those reported by Tseng and Fu (2017), albeit the fractional values are slightly different. The annual TTL cloud fractions within CA, SA, CP, and WP are 17%, 16%, 18%, and 20%, respectively. Clear seasonal variations are also noticed; during the boreal winter, the regional average fractions are increased to 24%, 24%, 27%, and 32%, respectively.

Then, monthly variations in the TTL CTH and associated TH are examined. Fig. 3 depicts the time series of the monthly mean TTL CTH (dashed lines) and corresponding TH (solid lines) over the four regions. All variables show clear seasonal variations; THs and TTL CTHs are higher during the boreal winter than in other seasons, and lowest THs and TTL CTHs are found during the boreal summer. Such variations further suggest the necessity and importance of considering more accurate THs instead of using a fixed TH value for TTL cloud study. The annual means of CTH and TH are approximately 16.83 km and 16.36 km, respectively, giving TTL CTH average higher than TH average by ~0.5 km.

Because of abundant TTL clouds over the selected four analysis domains and clear representation of land and ocean by four regions during the boreal winter, we consider the boreal winter period to examine TTL cloud properties, radiative heating/cooling effect, and cloud-forced vertical motion. Thus, hereafter, we present the results of four-year boreal winter mean fields.

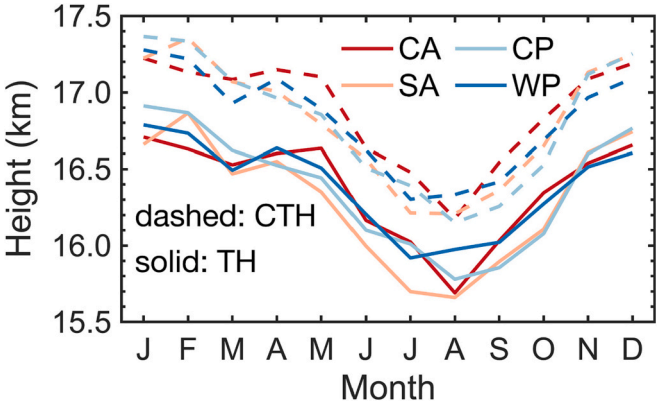

Fig. 3. Monthly and regional average TTL cloud top heights (CTH, dashed lines) and tropopause heights (TH, solid lines) over the four regions of interest.

Fig. 4 illustrates probability distributions of CTH, CBH, CD, and logarithmic IWP for different TTL cloud types. The top panels are for all TTL clouds, and the remaining three panels are for TTL DCCs, thick anvil clouds, and thin cirrus clouds, respectively. The CTHs for the total cloud, which are mainly located between 15 and 19 km (Fig. 4a), show very similar features amongst four regions although land areas (CA and SA) show slightly lower occurrences between 16.5 km and 18 km. The slight difference at those altitudes appears due to the more abundant DCCs over ocean regions (Fig. 4b). The CBH shows two peaks (Fig. 4e). The main peak located at approximately 16 km appears caused by abundant TTL cirrus clouds (Fig. 4h) while the secondary peak shown between 0 and 2 km is due to DCCs (Fig. 4f). In the CD probability distributions, anvil clouds and cirrus clouds show very similar distributions between land and ocean whereas a clear contrast is noted in DCC between land and ocean (Figs. 4i–l). Obvious differences are noticed between DCC CD distribution over land and ocean. Figs. 4m–p illustrate the CALIOP-derived IWPs probability distribution. In Fig. 4m, over the IWP range between 0.02 and 2 g/m^2, IWP over the WP region is relatively lower than other three regions, while, in the IWP range between 2 and 1000 g/m^2, WP shows higher IWP than others. Thus, over the WP regions, there seem to be more DCCs and anvil clouds, and less cirrus clouds, which can be explained by more frequent convections over the WP region. Noted that Fig. 4 displays probability distributions for DCC, anvil cloud, and cirrus cloud, representing their respective mean distributions. However, the total cloud distribution takes into account the occurrence frequency of each cloud type. Since the cloud amount of each type can differ, their respective weights must be considered to derive the total distribution. Thus, the probability distribution of WP region shows to be different from others.

As a summary, mean features of different types of TTL clouds are

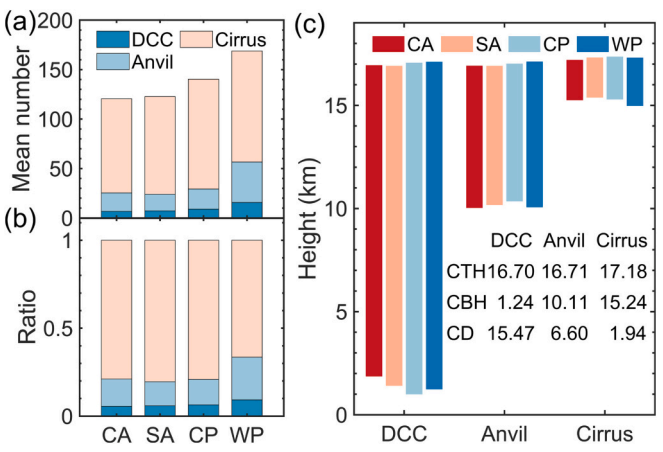

Fig. 5. (a) Absolute numbers of TTL cloudy pixels per unit area (within a 1° × 1° grid), (b) ratios of pixel numbers of different TTL cloudy types to their total, and (c) CTH, CBH and CD values for different cloud types over the four regions of interest in boreal winter from 2007 to 2010.

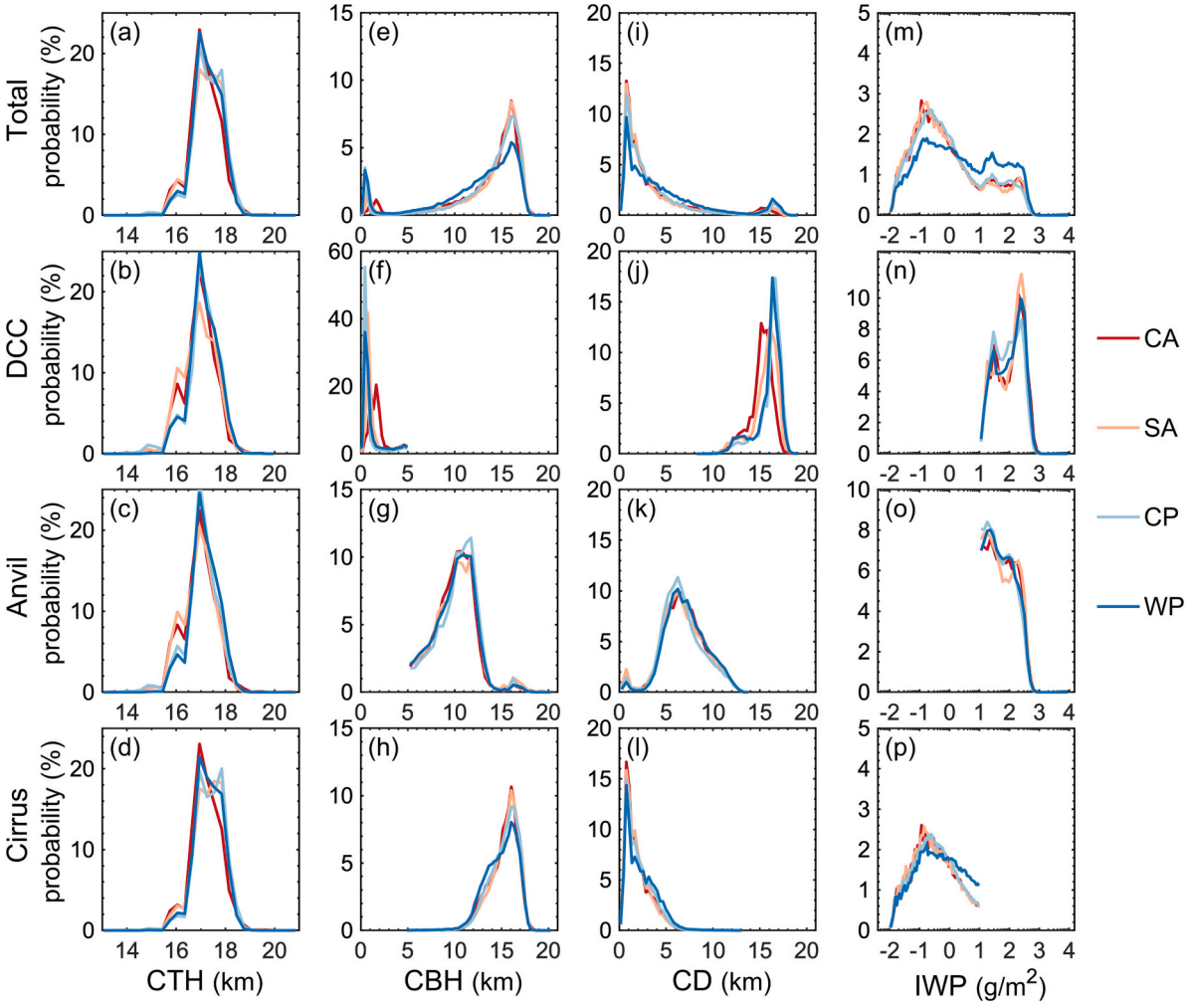

Fig. 4. Probability distribution of regional mean CTH, cloud base height (CBH), cloud depth (CD) and logarithmic IWP for all TTL clouds (top panels), as well as those for three types of TTL clouds (deep convective clouds, thick anvil clouds and thin cirrus clouds) in boreal winter from 2007 to 2010.

provided in Fig. 5. The absolute TTL cloud occurrences (i.e., TTL cloudy pixel numbers per unit area of 1° × 1° grid) are given in Fig. 5a for different cloud types at four analysis regions. Their respective ratios are given in Fig. 5b. Clearly, there are more TTL clouds over two ocean regions than those over land regions and especially TTL clouds are most abundant in WP (Fig. 5a), consistent with results from previous studies (Pilewskie and L'Ecuyer, 2022; Wang and Dessler, 2012). Interestingly, DCC and anvil cloud occurrences are more prevalent over the WP.

In terms of the ratio of each cloud to the total cloud occurrence, 76% of TTL clouds are thin cirrus clouds, and 17% are thick anvil clouds (Fig. 5b). Thus, in average sense, ~6.8% of TTL clouds are DCCs. While similar ratios are found CA, SA, and CP regions, the DCC fraction is the largest over the WP region, i.e., ~9.3%. At the same time, thick anvil clouds are the most abundant over the WP region, compared to other three regions (compare 24.3% for WP vs. 17% on average). As previously discussed, the classified thin cirrus clouds occupying about 76% of TTL clouds should be contributed by both in situ cirrus clouds and dissipating anvil clouds.

Vertically aligned geometrical feature of each type of TTL clouds is examined at four analysis domains (Fig. 5c). The vertical color bar represents the vertical extent of each type of cloud, and its top and bottom indicate CTH and CBH for each cloud, respectively. Thus, the difference (i.e., CTH minus CBH) represents the cloud depth CD. The mean values of four CTHs, CBHs and CDs are also provided in Fig. 5c. It is shown that CTHs of TTL cirrus clouds (i.e., 17.18 km) are slightly higher than those of TTL DCCs (i.e., 16.70 km), and also higher than those of anvil clouds (i.e., 16.71 km). It is interesting to note that the CTHs over the ocean regions are slightly higher than those over the land regions, especially for DCCs and anvil clouds, although the CTH differences between land and ocean are mostly small, i.e., < 0.2 km.

The CBHs for DCCs over land are higher than those over ocean, which is largely due to the topographical effects over the land. The mean CDs for thin cirrus cloud, thick anvil cloud and DCC are 1.94 km, 6.60 km and 15.47 km, respectively. It is noted that anvil clouds classified in this study are geometrically thick (6.60 km) as well as optically thick (IWC > 10 g/m^2), and therefore thick anvil clouds here are considered not cirrus clouds but convectively-driven anvil clouds. Since the convectively-driven anvil clouds eventually dissipate into optically and geometrically thinner cirrus-type clouds, the cirrus clouds defined in this study should be consisted of in situ cirrus clouds and cirrus clouds dissipating from anvil clouds. However, considering that the mean CTHs of the cirrus clouds are higher than DCCs and anvil clouds (17.18 km vs. 16.70 km and 16.71 km), the cirrus clouds should be dominated by in situ cirrus clouds. It is because the CTHs of cirrus clouds from dissipating anvil clouds are likely similar or lower due to the subsiding environment, compared to those for DCCs and anvil clouds.

4. Cloud-induced radiative heating and associated vertical velocity

In order to examine the impact of TTL clouds on the radiative heating in the TTL and then on the upwelling motion, shortwave (SW) and longwave (LW) radiative heating rates generated by DCCs, anvil clouds, and cirrus clouds are illustrated in Fig. 6, along with radiative heating rate profile for the clear sky. Note that Fig. 6 is only for the daytime, and the radiative heating rates in Fig. 6 represent the mean radiative heating rate over the area occupied by each cloud type or clear sky. During the daytime, the largest radiative heating rate for SW (up to 15 K/day) can be generated in deep convection conditions over the land (DCCs for CA and SA) at approximately 15.5 km level. Meanwhile, the radiative heating rates over the ocean regions are approximately half at the land's peak heating level. Such large difference in the radiative heating is likely due to the convection intensity between land and ocean; stronger convection over the land can carry more of cloud's hydrometeors upward to the tropopause level, allowing more solar absorption over the land.

Compared with DCCs, radiative heating rates for anvil and cirrus clouds are much smaller, i.e., around 1.5 K at approximately 15.5 km level (Figs. 6b–c). It is noted that cloud-induced radiative heating rates are consistent amongst three cloud types, i.e., broad radiative heating throughout the TTL and around the tropopause. In contrast, radiative heating magnitudes in clear-sky conditions are much smaller, suggesting that the SW radiative heating for the cloudy conditions are mainly from the solar absorption by clouds.

For LW radiative heating rates during the daytime (Figs. 6e–h), the DCC-induced radiative cooling pattern is somewhat opposite to warming patterns for anvil clouds, cirrus clouds and clear sky conditions in the TTL, despite the LW radiative cooling below approximately 15 km under these circumstances. The LW daytime radiative cooling by DCCs is found

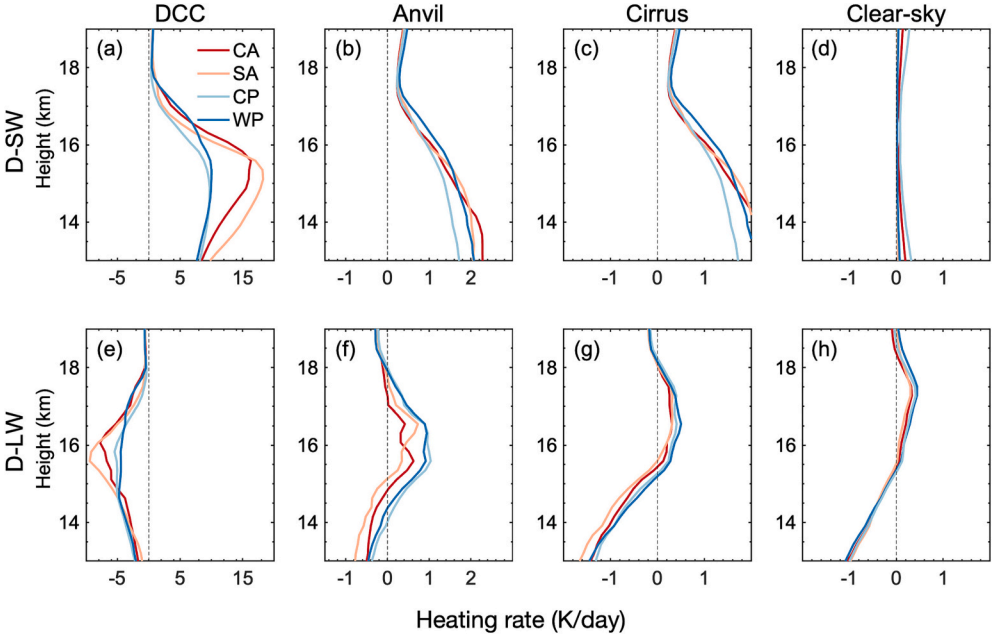

Fig. 6. Average radiative heating rates of shortwave (SW) and longwave (LW) components during daytime for three different cloud types, i.e., DCCs, anvil clouds, and cirrus clouds, and for the clear sky in the boreal winter from 2007 to 2010.

to be also opposite to the SW radiative heating by DCCs, but with a much smaller magnitude.

The daytime net radiative heating rates are obtained by taking an average of SW and LW radiative heating rates given in Fig. 6, and are presented in Figs. 7a–d. Also provided in Fig. 7 are clouds and clear-sky induced vertical velocities (Figs. 7e–h). Note that the vertical velocity is the p-velocity given in unit of Pa/s. As described in Section 2.3, the positive radiative heating corresponds to upwelling motion, i.e., negative vertical velocity in the p-coordinate. It is noted that net radiative heating induced by any TTL cloud is positive during the daytime. The DCC-induced radiative heating (Fig. 7a) mainly occurs below approximately 16 km, and magnitudes are much larger over land (up to 10 K/day) than that over ocean. Anvil cloud tends to generate relatively larger radiative heating below 17 km. The radiative heating by cirrus cloud is relatively smaller than 1 K/day and situates broadly over the entire TTL layer. Interestingly, the maximum radiative heating contribution layers (i.e., the level of maximum radiative heating) become lower from clear sky to cirrus clouds, anvil clouds, and DCCs in order, indicating that all TTL clouds can lower the zero heating rate level shown in the clear sky at approximately 15 km.

The vertical velocities for three cloudy conditions and clear sky (Figs. 7e–h) show that the largest vertical velocity is from DCCs, whose magnitudes are in the range of 0.01–0.03 Pa/s (0.002 Pa/s is equivalent to ~1.5 mm/s). Anvil-induced vertical velocity appears one order smaller than that for DCCs, and vertical velocities induced by cirrus clouds and clear sky appear to be much smaller during the daytime. It is interesting to note that the magnitudes of both radiative heating and vertical velocity are larger over ocean than those over land within most of the TTL, consistent with the result of Pilewskie and L'Ecuyer (2022). This is probably due to the more frequent development of convective systems over ocean, compared to more isolated convection systems over land. However, as expected, there is less discernible clear-sky radiative heating between land and ocean.

Nighttime radiative heating and vertical velocity induced by clouds and clear sky are obtained and given in Fig. 8. Compared with daytime LW radiative heating distributions (Figs. 6e–h), radiative heating rates for nighttime LW are very similar to those found in daytime, although DCC-induced radiative cooling during the nighttime is slightly smaller at approximately 16 km. Compared with daytime net radiative heating results (Fig. 7), because of absent solar radiation, cloud-induced vertical distribution is quite different below 15 km, where downwelling motions are generated by all three clouds. In particular, large changes in DCC-generated velocities are shown with a sign change (from strong updraft to downwelling), when daytime and nighttime are compared.

So far cloud-induced radiative heating and vertical velocity are the values for cloud-occupying areas only. Since TTL cloud occurrence frequencies vary with region, the regional radiative heating and associated vertical motion are estimated by taking the occurrence frequencies of TTL clouds into account. Obtained radiative heating distributions and associated vertical velocities for averaged nighttime and daytime are given in Fig. 9.

The regional average of radiative heating in the cloudy conditions (Fig. 9a) indicates radiative heating above approximately 14.5 km, with a maximum at approximately 15.5 km (with a radiative heating rate of about 0.7 K/day). Radiative cooling is dominant below the altitude of about 14.5 km. These features establish an overall radiative heating layer between approximately 14.5 km and 18 km. Compared to the clear-sky radiative heating distribution in Fig. 9b, it is clear that cloud can lower the zero net radiative heating rate level at 15.5 km shown in the clear sky. The lowering of the zero net radiative heating rate level should have been achieved by dominant radiative heating influences of TTL clouds below about 17 km (Fig. 9c). We further note that comparatively larger magnitudes of radiative heating are found over oceanic regions than those over land counterparts (Fig. 9a), mainly because of more abundant anvil and cirrus clouds in the ocean regions (see Fig. 5a). The derived vertical velocity distributions suggest that the upward motion revealed in the clear sky above approximately 15.5 km (Fig. 9e) can be intensified by cloud-induced upward motion given in Fig. 9f. Because of the cloud influence on vertical motion, the upward motions in the cloudy conditions are established with a stronger magnitude above approximately 14.5 km.

In addition, it is also noted that oceanic radiative heating due to clouds is larger than the land counterparts, especially for the WP. Considering that clear-sky radiative heating is not so different between the land and ocean (Fig. 9b), it is the cloud presence that shapes the differences noted in the cloudy-sky radiative heating distribution.

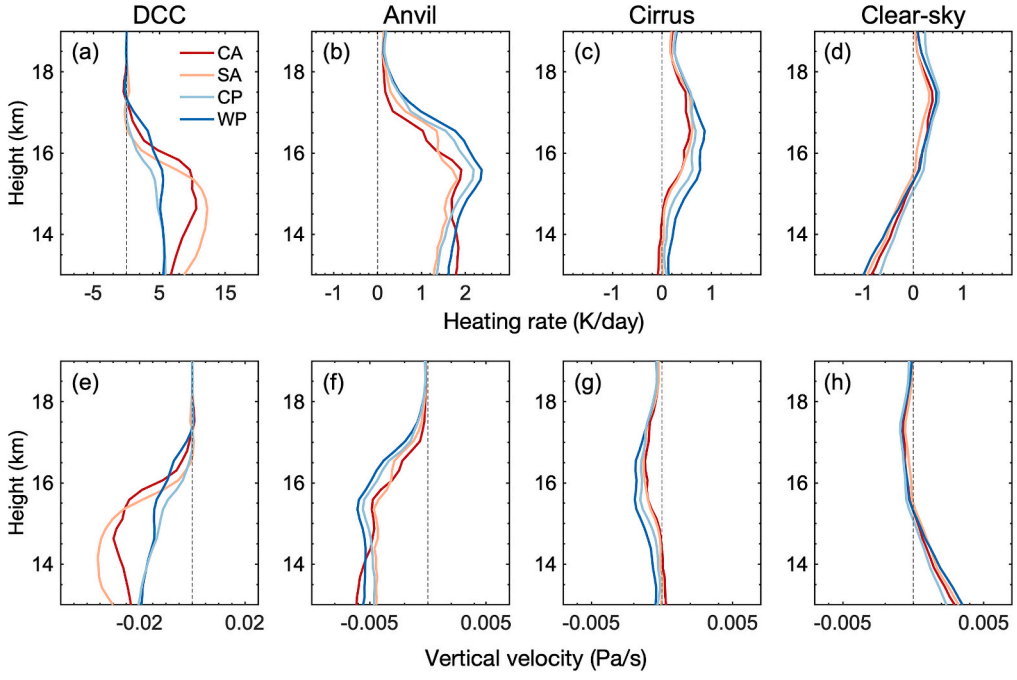

Fig. 7. Average net radiative heating rate and corresponding vertical velocity during the daytime for three kinds of TTL clouds and clear sky in boreal winter from 2007 to 2010.

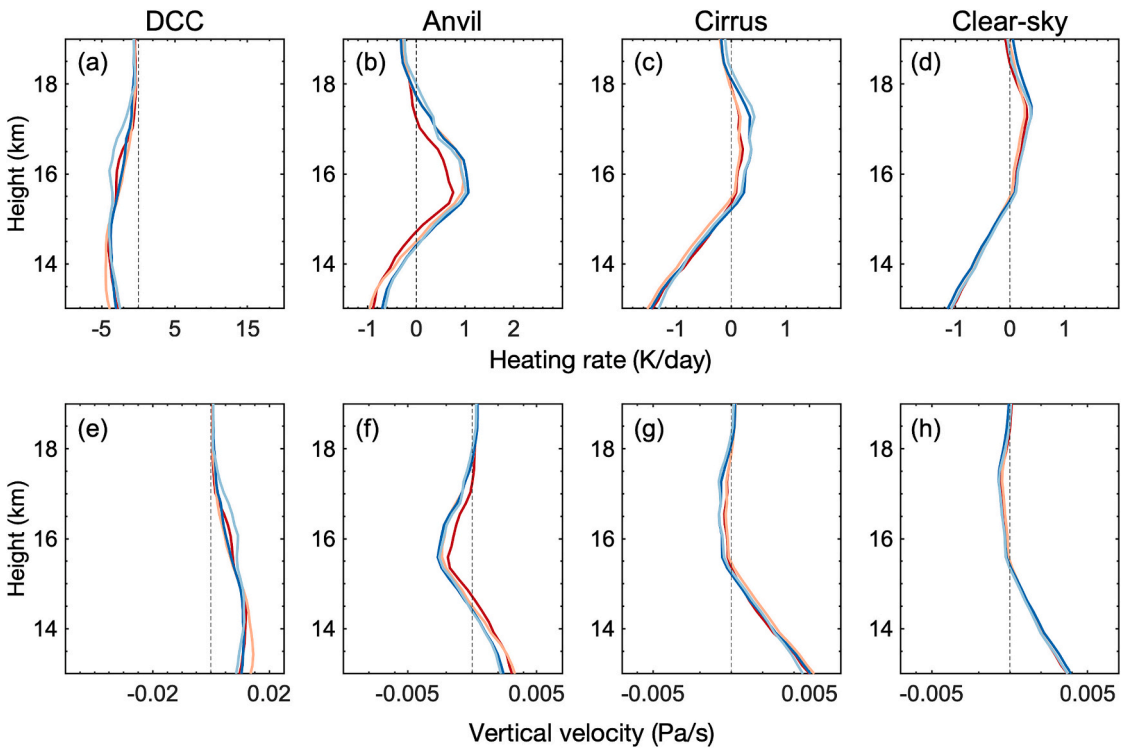

Fig. 8. Same as Fig. 7 but during the nighttime.

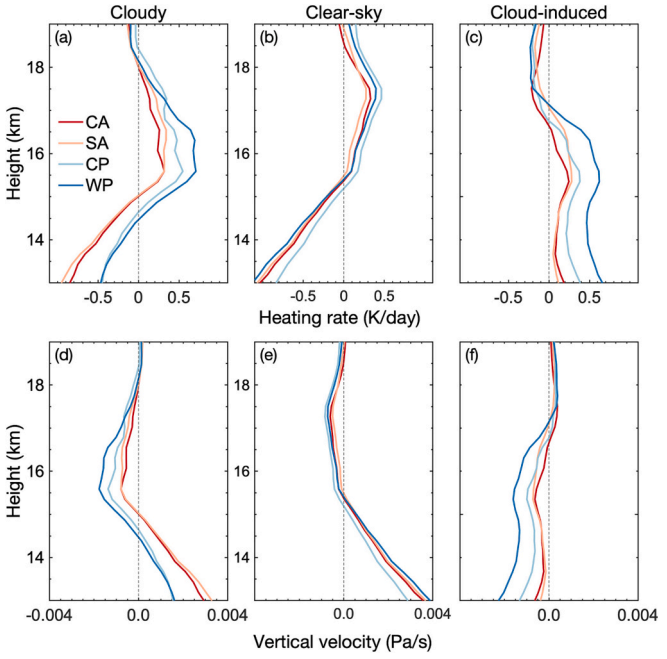

Fig. 9. Regional average radiative heating rates (top panel) and vertical velocities (bottom panel) for cloudy sky, clear sky and cloud-induced (cloudy *minus* clear) conditions in boreal winter from 2007 to 2010.

Furthermore, as indicated in the individual cloud proportion (Fig. 5b) and the associated radiative heating distributions (Fig. 7), anvil and cirrus clouds should have contributed the most to the radiative heating distribution in the cloud conditions since their radiative heating rate behaves similarly to that of cloudy radiative heating (Fig. 9a). Amongst TTL clouds, the radiative heating induced by cirrus clouds is found to be the largest because its largest proportion to total TTL clouds (i.e., 76% of the total TTL clouds as shown in Fig. 5b).

5. Summary and discussion

This study examines statistical properties of TTL clouds as well as the radiatively induced vertical motions by classified TTL cloud types, using combined active spaceborne lidar (CALIPSO) and radar (CloudSat) data over four years (2007–2010). We focus on four regions of CA, SA (continental regions), CP and WP (oceanic regions) over the tropics during the boreal winter. In this study, TTL clouds are defined as cloudy pixels whose CTHs are located above local THs. Those selected TTL clouds are classified into three types (i.e., DCCs, thick anvil clouds, and thin cirrus clouds) based on CALIOP-estimated IWP and cloud geometrical structure. This classification resulted in clear differences in the mean cloud depth, i.e., 1.94, 6.60, and 15.47 km for cirrus cloud, anvil cloud, and DCC. Since the TTL cirrus clouds are from in situ as well as from dissipating anvil clouds, the anvil cloud defined in this study should be convectively-driven thick anvil clouds. Thus, the cirrus clouds here are composed of in situ cirrus clouds and thin cirrus clouds from dissipating anvil clouds.

About 76% of the total TTL clouds are found to be cirrus clouds, but the proportion by each cirrus cloud type cannot be directly estimated. However, considering that the mean CTH of cirrus clouds is 17.18 km while mean CTHs for anvil clouds and DCCs are 16.71 km and 16.70 km, respectively, the cirrus clouds are dominantly contributed by in situ cirrus clouds. It is because the dissipating anvil clouds are generally subject to sinking environmental conditions, and thus the cloud CTH of the anvil-originated cirrus clouds should be similar to or lower than 16.71 km. Only way to explain higher CTH (17.18 km) should be abundant in situ cirrus clouds whose CTHs are higher than anvil-originated cirrus clouds. Previous studies indicated that in situ cirrus clouds occupy slightly more than half of the total cirrus clouds (Luo and Rossow, 2004; Heymsfield and Donner, 1990). However, this study suggests that in situ cirrus is far dominant in cirrus cloud in TTL over the tropics.

In order to examine the TTL cloud influences on the upward motion,

radiative heating profiles contributed by different types of TTL cloud and their derived upwelling velocities are obtained. The radiative heating rates indicate that thin cirrus clouds are the most dominant contributor to the overall radiative heating rate (~48.4% on average for the layer of approximately 15.5 km) due to abundant cirrus clouds. Note that, amongst classified three types of TTL clouds, cirrus clouds occupy nearly 76% of the total, and approximately 17% and 7% are anvil clouds and DCCs, respectively. In spite of the dominance of cirrus cloud contribution, it is also clear that the contributions by anvil clouds and DCCs to the total radiative heating are significant.

The overall radiative heating by TTL clouds indicates that TTL clouds can lower the level of zero net radiative heating rate shown in the clear-sky condition, by approximately 400–900 m (400 m over land and 900 m over ocean). The lowering effect appears to establish broad radiative heating layer from the upper troposphere to the TTL. Such changes in radiative heating distributions further indicate that upwelling can be induced by the presence of TTL clouds themselves despite the fact that the TTL clouds are produced with underlying circulation. The TTL upwelling magnitude in the 14–18 km layer reaches 0.002 Pa/s (equivalent to ~1.5 mm/s at 100 hPa) over the WP, where the TTL clouds are most abundant. Considering that the mean upwelling at 100 hPa level over the tropics is ~0.5 mm/s (Randel et al., 2008; Kim et al., 2016), cloud-induced upwelling in the TTL is thought to be significant to maintain the continuous updraft motion in the TTL. It may take approximately ~10–15 days to move those gas in clouds from approximately 15.5 km to 16.8 km (averaged CTH shown in Fig. 3) inferred from only vertical velocity induced by radiative heating rate. The radiation-driven upwelling motion is a rather slow process, and it may be masked by stronger adiabatic processes (i.e., wave). Since cloud-induced radiative heating is attributed not only to cirrus clouds but also to anvil clouds and DCCs, upwelling should be understood collectively but with different types of clouds.

In addition, the cloud-induced upwelling obtained in this study may help to understand the role of the WP as a dominant contributor in transporting air to the TTL and to the stratosphere (Fueglistaler et al., 2004). The results may support the role of TTL clouds in transporting air from the troposphere to the stratosphere by linking the fast ascending convection regime to the slow ascending Brewer–Dobson circulation regime above the TTL (Corti et al., 2006).

CRediT authorship contribution statement

Siliang Lei: Conceptualization, Methodology, Software, Investigation, Formal analysis, Data curation, Visualization, Writing – original draft, Writing – review & editing. **Byung-Ju Sohn:** Conceptualization, Methodology, Formal analysis, Supervision, Funding acquisition, Resources, Writing – review & editing. **Joowan Kim:** Investigation, Writing – review & editing. **Chao Liu:** Resources, Project administration, Supervision, Funding acquisition, Writing – review & editing.

Declaration of Competing Interest

The authors declare that they have no known competing financial interests or personal relationships that could have appeared to influence the work reported in this paper.

Data availability

Data will be made available on request.

Acknowledgments

We acknowledge the funding supported by the National Natural Science Foundation of China (42122038) and the Postgraduate Research and Practice Innovation Program of Jiangsu Province (KYCX22_1169). BJS was supported by the National Research Foundation of Korea (NRF) under Grant NRF-2021R1A4A5032320. The simulations are conducted in the High Performance Computing Center of Nanjing University of Information Science & Technology. All data in this work are publicly available online for all researchers. The CALIOP version 4.20 vertical feature mask (VFM) and 05kmCPro are both available from https://subset.larc.nasa.gov/calipso/login.php. The CloudSat cloud classification product is acquired through the CloudSat Data Processing Center and can be accessed from http://www.cloudsat.cira.colostate.edu. The CALIPSO-CloudSat P1_R05 2B-FLXHR-LIDAR and R05 ECMWF-AUX products are both downloaded at https://www.icare.univ-lille.fr/. DARDAR-CLOUD v2.1.1 data are obtained from the AERIS/ICARE Data and Services Center (http://www.icare.univ-lille1.fr/projects/dardar).

References

Ceccaldi, M., Delanoë, J., Hogan, R.J., Pounder, N.L., Protat, A., Pelon, J., 2013. From CloudSat-CALIPSO to EarthCare: Evolution of the DARDAR cloud classification and its comparison to airborne radar-lidar observations: Evolution of DARDAR classification. J. Geophys. Res.-Atmos. 118, 7962–7981. https://doi.org/10.1002/jgrd.50579.

Chang, K., L'Ecuyer, T.S., 2019. Role of latent heating vertical distribution in the formation of the tropical cold trap. J. Geophys. Res.-Atmos. 124, 7836–7851. https://doi.org/10.1029/2018JD030194.

Corti, T., Luo, B.P., Peter, T., Vömel, H., Fu, Q., 2005. Mean radiative energy balance and vertical mass fluxes in the equatorial upper troposphere and lower stratosphere. Geophys. Res. Lett. 32, L06802. https://doi.org/10.1029/2004GL021889.

Corti, T., Luo, B.P., Fu, Q., Vomel, H., Peter, T., 2006. The impact of cirrus clouds on tropical troposphere-to-stratosphere transport. Atmos. Chem. Phys. 6, 2539–2547. https://doi.org/10.5194/acp-6-2539-2006.

[dataset] Cronk, H., Partain, P., 2017. CloudSat ECMWF-AUX Auxiliary Data Product Process Description and Interface Control Document. NASA. ECMWF-AUX_PDICD.P_R05.rev0, 4pp.

Delanoë, J., Hogan, R.J., 2010. Combined CloudSat-CALIPSO-MODIS retrievals of the properties of ice clouds. J. Geophys. Res.-Atmos. 115, D00H29. https://doi.org/10.1029/2009JD012346.

Fu, Q., Smith, M., Yang, Q., 2018. The impact of cloud radiative effects on the tropical tropopause layer temperatures. Atmosphere. 9 (10), 377. https://doi.org/10.3390/atmos9100377.

Fueglistaler, S., Wernli, H., Peter, T., 2004. Tropical troposphere-to-stratosphere transport inferred from trajectory calculations: Tropical troposphere-to-stratosphere transport. J. Geophys. Res.-Atmos. 109, D03108. https://doi.org/10.1029/2003JD004069.

Fueglistaler, S., Dessler, A.E., Dunkerton, T.J., Folkins, I., Fu, Q., Mote, P.W., 2009. Tropical tropopause layer. Rev. Geophys. 47, RG1004. https://doi.org/10.1029/2008RG000267.

Garrett, T.J., Heymsfield, A.J., McGill, M.J., Ridley, B.A., Baumgardner, D.G., Bui, T.P., Webster, C.R., 2004. Convective generation of cirrus near the tropopause: Cirrus near the tropopause. J. Geophys. Res.-Atmos. 109, D21203. https://doi.org/10.1029/2004JD004952.

Gettelman, A., de F Forster, P.M., Fujiwara, M., Fu, Q., Vömel, H., Gohar, L.K., Johanson, C., Ammerman, M., 2004. Radiation balance of the tropical tropopause layer. J. Geophys. Res. 109, D07103. https://doi.org/10.1029/2003JD004190.

Haladay, T., Stephens, G., 2009. Characteristics of tropical thin cirrus clouds deduced from joint CloudSat and CALIPSO observations. J. Geophys. Res. 114, D00A25. https://doi.org/10.1029/2008JD010675.

Harrop, B.E., Hartmann, D.L., 2016. The role of cloud radiative heating in determining the location of the ITCZ in Aquaplanet simulations. J. Clim. 29, 2741–2763. https://doi.org/10.1175/JCLI-D-15-0521.1.

Hartmann, D.L., Holton, J.R., Fu, Q., 2001. The heat balance of the tropical tropopause, cirrus, and stratospheric dehydration. Geophys. Res. Lett. 28, 1969–1972. https://doi.org/10.1029/2000GL012833.

Henderson, D.S., L'Ecuyer, T., Stephens, G., Partain, P., Sekiguchi, M., 2013. A multisensor perspective on the radiative impacts of clouds and aerosols. J. Appl. Meteorol. Climatol. 52, 853–871. https://doi.org/10.1175/JAMC-D-12-025.1.

Heymsfield, A.J., Donner, L.J., 1990. A scheme for parameterizing ice-cloud content in general circulation models. J. Atmos. Sci. 47, 1865–1877. https://doi.org/10.1175/1520-0469(1990)047<1865:ASFPIC>2.0.CO;2.

Heymsfield, G.M., Tian, L., Heymsfield, A.J., Li, L., Guimond, S., 2010. Characteristics of deep tropical and subtropical convection from nadir-viewing high-altitude airborne doppler radar. J. Atmos. Sci. 67, 285–308. https://doi.org/10.1175/2009JAS3132.1.

Huaman, L., Schumacher, C., 2018. Assessing the vertical latent heating structure of the East Pacific ITCZ using the CloudSat CPR and TRMM PR. J. Clim. 31, 2563–2577. https://doi.org/10.1175/JCLI-D-17-0590.1.

Jensen, E.J., Toon, O.B., Selkirk, H.B., Spinhirne, J.D., Schoeberl, M.R., 1996. On the formation and persistence of subvisible cirrus clouds near the tropical tropopause. J. Geophys. Res.-Atmos. 101, 21361–21375. https://doi.org/10.1029/95JD03575.

Jeyaratnam, J., Luo, Z.J., Giangrande, S.E., Wang, D., Masunaga, H., 2021. A satellite-based estimate of convective vertical velocity and convective mass flux: Global survey and comparison with radar wind profiler observations. Geophys. Res. Lett. 48 https://doi.org/10.1029/2020GL090675.

Kim, J., Randel, W.J., Birner, T., Abalos, M., 2016. Spectrum of wave forcing associated with the annual cycle of upwelling at the tropical tropopause. J. Atmos. Sci. 73, 855–868. https://doi.org/10.1175/JAS-D-15-0096.1.

Lawson, R.P., Woods, S., Jensen, E., Erfani, E., Gurganus, C., Gallagher, M., Connolly, P., Whiteway, J., Baran, A.J., May, P., Heymsfield, A., Schmitt, C.G., McFarquhar, G., Um, J., Protat, A., Bailey, M., Lance, S., Muehlbauer, A., Stith, J., Korolev, A., Toon, O.B., Krämer, M., 2019. A review of ice particle shapes in cirrus formed in situ and in anvils. J. Geophys. Res.-Atmos. 124, 10049–10090. https://doi.org/10.1029/2018JD030122.

Lucas, C., Zipser, E.J., Lemone, M.A., 1994. Vertical velocity in oceanic convection off tropical Australia. J. Atmos. Sci. 51, 3183–3193. https://doi.org/10.1175/1520-0469(1994)051<3183:VVIOCO>2.0.CO;2.

Luo, Z., Rossow, W.B., 2004. Characterizing tropical cirrus life cycle, evolution, and interaction with upper-tropospheric water vapor using lagrangian trajectory analysis of satellite observations. J. Clim. 17, 4541–4563. https://doi.org/10.1175/3222.1.

Mapes, B.E., Houze, J.R.A., 1995. Diabatic divergence profiles in western Pacific mesoscale convective systems. J. Atmos. Sci. 52 (10), 1807–1828. https://doi.org/10.1175/1520-0469(1995)052<1807:DDPIWP>2.0.CO;2.

Matsui, T., Chern, J.-D., Tao, W.-K., Lang, S., Satoh, M., Hashino, T., Kubota, T., 2016. On the land–ocean contrast of tropical convection and microphysics statistics derived from TRMM satellite signals and global storm-resolving models. J. Hydrometeorol. 17, 1425–1445. https://doi.org/10.1175/JHM-D-15-0111.1.

Mauritsen, T., Graversen, R.G., Klocke, D., Langen, P.L., Stevens, B., Tomassini, L., 2013. Climate feedback efficiency and synergy. Clim. Dyn. 41, 2539–2554. https://doi.org/10.1007/s00382-013-1808-7.

Olson, W.S., Kummerow, C.D., Hong, Y., Tao, W.K., 1999. Atmospheric latent heating distributions in the tropics derived from satellite passive microwave radiometer measurements. J. Appl. Meteorol. 38, 633–664. https://doi.org/10.1175/1520-0450(1999)038<0633:ALHDIT>2.0.CO;2.

Pan, L.L., Munchak, L.A., 2011. Relationship of cloud top to the tropopause and jet structure from CALIPSO data. J. Geophys. Res. 116, D12201. https://doi.org/10.1029/2010JD015462.

Pilewskie, J.A., L'Ecuyer, T.S., 2022. The global nature of early-afternoon and late-night convection through the eyes of the A-Train. J. Geophys. Res.-Atmos. 127 https://doi.org/10.1029/2022JD036438.

Randel, W.J., Garcia, R., Wu, F., 2008. Dynamical balances and tropical stratospheric upwelling. J. Atmos. Sci. 65, 3584–3595. https://doi.org/10.1175/2008JAS2756.1.

[dataset] Rienecker, M., 2008. File specification for GEOS-5 DAS gridded output. NASA. Tech. Rep., GMAO-1001v6.4, 54 pp.

Sobel, A.H., Nilsson, J., Polvani, L.M., 2001. The weak temperature gradient approximation and balanced tropical moisture waves. J. Atmos. Sci. 58 (23), 3650–3665. https://doi.org/10.1175/1520-0469(2001)058<3650:TWTGAA>2.0.CO;2.

Sohn, B.-J., 1999. Cloud-induced infrared radiative heating and its implications for large-scale tropical circulations. J. Atmos. Sci. 56, 2657–2672. https://doi.org/10.1175/1520-0469(1999)056<2657:CIIRHA>2.0.CO;2.

Sokol, A.B., Hartmann, D.L., 2020. Tropical anvil clouds: radiative driving toward a preferred state. J. Geophys. Res.-Atmos. 125 https://doi.org/10.1029/2020JD033107 e2020JD033107.

Stephens, G.L., Vane, D.G., Boain, R.J., Mace, G.G., Sassen, K., Wang, Z., Illingworth, A. J., O'connor, E.J., Rossow, W.B., Durden, S.L., Miller, S.D., Austin, R.T., Benedetti, A., Mitrescu, C., the CloudSat Science Team, 2002. The CloudSat mission and the A-Train: a new dimension of space-based observations of clouds and precipitation. Bull. Am. Meteorol. Soc. 83, 1771–1790. https://doi.org/10.1175/BAMS-83-12-1771.

Stephens, G.L., Vane, D.G., Tanelli, S., Im, E., Durden, S., Rokey, M., Reinke, D., Partain, P., Mace, G.G., Austin, R., L'Ecuyer, T., Haynes, J., Lebsock, M., Suzuki, K., Waliser, D., Wu, D., Kay, J., Gettelman, A., Wang, Z., Marchand, R., 2008. CloudSat mission: Performance and early science after the first year of operation. J. Geophys. Res. 113 (D00A18), D00A18. https://doi.org/10.1029/2008JD009982.

Tegtmeier, S., Anstey, J., Davis, S., Dragani, R., Harada, Y., Ivanciu, I., Pilch Kedzierski, R., Krüger, K., Legras, B., Long, C., Wang, J.S., Wargan, K., Wright, J.S., 2020. Temperature and tropopause characteristics from reanalyses data in the tropical tropopause layer. Atmos. Chem. Phys. 20, 753–770. https://doi.org/10.5194/acp-20-753-2020.

Tseng, H.H., Fu, Q., 2017. Tropical tropopause layer cirrus and its relation to tropopause. J. Quant. Spectrosc. Radiat. Transf. 188, 118–131. https://doi.org/10.1016/j.jqsrt.2016.05.029.

[dataset] Vaughan, M., Pitts, M., Trepte, C., Winker, D., Detweiler, P., Garnier, A., Getzewich, B., Hunt, W., Lambeth, J., Lee, K., Tremas, T., Bazureau, A., Pelon, J., 2018. Cloud–Aerosol LIDAR Infrared Pathfinder Satellite Observations Data Management System Data Products Catalog. NASA Langley Research Center. CALIPSO_DPC_Rev4x30, 97pp.

Virts, K.S., Wallace, J.M., 2010. Annual, interannual, and intraseasonal variability of tropical tropopause transition layer cirrus. J. Atmos. Sci. 67, 3097–3112. https://doi.org/10.1175/2010JAS3413.1.

Virts, K.S., Wallace, J.M., Fu, Q., Ackerman, T.P., 2010. Tropical tropopause transition layer cirrus as represented by CALIPSO lidar observations. J. Atmos. Sci. 67, 3113–3129. https://doi.org/10.1175/2010JAS3412.1.

Wang, T., Dessler, A.E., 2012. Analysis of cirrus in the tropical tropopause layer from CALIPSO and MLS data: a water perspective: TTL convective cirrus. J. Geophys. Res.-Atmos. 117, D04211. https://doi.org/10.1029/2011JD016442.

Winker, D.M., Pelon, J., Coakley, J.A., Ackerman, S.A., Charlson, R.J., Colarco, P.R., Flamant, P., Fu, Q., Hoff, R.M., Kittaka, C., Kubar, T.L., Le Treut, H., Mccormick, M. P., Mégie, G., Poole, L., Powell, K., Trepte, C., Vaughan, M.A., Wielicki, B.A., 2010. The CALIPSO mission. Bull. Am. Meteorol. Soc. 91, 1211–1230. https://doi.org/10.1175/2010BAMS3009.1.

Xian, T., Homeyer, C.R., 2019. Global tropopause altitudes in radiosondes and reanalyses. Atmos. Chem. Phys. 19, 5661–5678. https://doi.org/10.5194/acp-19-5661-2019.

Yanai, M., Esbensen, S., Chu, J., 1973. Determination of bulk properties of tropical cloud clusters from large-scale heat and moisture budgets. J. Atmos. Sci. 30, 611–627. https://doi.org/10.1175/1520-0469(1973)030<0611:DOBPOT>2.0.CO;2.

Yang, S., Smith, E.A., 2000. Vertical structure and transient behavior of convective–stratiform heating in TOGA COARE from combined satellite–sounding analysis. J. Appl. Meteorol. 39, 1491–1513. https://doi.org/10.1175/1520-0450(2000)039%3c1491:VSATBO%3e2.0.CO;2.

Yang, Q., Fu, Q., Hu, Y., 2010. Radiative impacts of clouds in the tropical tropopause layer. J. Geophys. Res. 115, D00H12. https://doi.org/10.1029/2009JD012393. D00H12.

Zipser, E.J., Cecil, D.J., Liu, C., Nesbitt, S.W., Yorty, D.P., 2006. Where are the most intensity thunderstorm on Earth? Bull. Am. Meteorol. Soc. 87, 1057–1072. https://doi.org/10.1175/BAMS-87-8-1057.